



CHORUS

This is the accepted manuscript made available via CHORUS. The article has been published as:

Unsteady sedimentation of a sphere in wormlike micellar fluids

Yiran Zhang and Susan J. Muller

Phys. Rev. Fluids **3**, 043301 — Published 9 April 2018

DOI: [10.1103/PhysRevFluids.3.043301](https://doi.org/10.1103/PhysRevFluids.3.043301)

Unsteady sedimentation of a sphere in wormlike micellar fluids

Yiran Zhang and Susan J. Muller*

Department of Chemical & Biomolecular Engineering, University of California, Berkeley

Abstract

The unsteady sedimentation of a sphere in wormlike micellar fluids is studied experimentally through shear and extensional rheometry, sphere trajectory tracking and particle image velocimetry. Unsteady sphere sedimentation characterized by fluctuations in the sphere settling velocity was observed for a range of sphere size and density in two non-shear-banding wormlike micellar solutions, a cetylpyridinium chloride (CpCl) - sodium salicylate (NaSal) solution and a cetyltrimethylammonium p-toluenesulfonate (CTAT) - NaCl solution. The onset of the transition from steady to unsteady sphere motion is characterized by an extensional Deborah number, De_{ext} , defined locally in the negative wake of the falling sphere. This instability criterion is in agreement with previous findings by Mohammadigoushki and Muller [J. Rheol. **60**, 1761 (2016)] in the wormlike micelle system of cetyltrimethylammonium bromide (CTAB) and NaSal, and appears to be universally valid independent of micelle chemistry or solution rheology (*e.g.* shear banding or not). Moreover, the frequency at which the sphere velocity fluctuates is found to be linearly correlated with an average shear Deborah number De_s , which is a measure of the overall flow strength. This suggests that a constant critical strain is accumulated before the flow instability takes place in each velocity oscillation. The velocity fluctuations are found to become increasingly disordered with increasing elastic Mach number, Ma_e , indicating that the interactions between the flow instability and elastic wave propagation result in more chaotic velocity fluctuations.

*Corresponding Author. Email: muller2@berkeley.edu

1. Introduction

The motion of a sphere falling through complex fluids has been extensively studied, both experimentally and theoretically [1]. It has become one of the benchmark problems to evaluate constitutive models of complex fluids and numerical calculations methods [2]. In addition, the sedimentation of a single, unbounded sphere is an important model system for many industrial processes involving the sedimentation of particle suspensions and flow past obstacles. In Newtonian fluids, Stokes [3] first studied an unbounded sphere settling at low Reynolds number ($Re = \rho_f V_s d / \eta \ll 1$, where ρ_f is the fluid density, V_s is the sphere terminal velocity, d is the sphere diameter and η is the fluid viscosity). In the absence of inertia, the flow around the falling sphere has fore-aft symmetry, and Stokes law ($F_\eta = 3\pi\eta d V_s$) relates the viscous drag force on the sphere, F_η , to the sphere steady terminal velocity, V_s . This relationship forms the basis of falling ball viscometry. In more complex fluids, the creeping flow around a sphere is modified by the fluid rheological properties, such as shear-rate-dependent viscosity and viscoelasticity, and the fore-aft symmetry of the flow is often lost [4]. In the past few decades, the effects of fluid rheology on sphere terminal velocity and the surrounding fluid flow has been widely researched with various complex fluids, including Boger fluids, shear-thinning polymer solutions, and wormlike micellar fluids.

For a sphere falling through viscoelastic, shear-thinning polymer solutions, it has been shown that a “negative wake” can form. The negative wake is a recirculation region downstream of the sphere, where the fluid velocity becomes opposite to the direction of the sphere motion. Both experimental results [5] and theoretical calculations [6,7] suggest that the formation of a negative wake is a result of a balance between stress relaxation due to the shear deformation around the moving sphere, and the elongational deformation in the wake. A criterion has been proposed [5–7] that the negative wake is present when the ratio of Deborah number De to Trouton ratio Tr is large. Here the Deborah number De characterizes the fluid viscoelasticity, and is defined as $De = \lambda \dot{\gamma}$, where λ is the fluid relaxation time and $\dot{\gamma}$ is the characteristic shear rate ($\dot{\gamma} = V_s / d$). The Trouton ratio Tr characterizes the extensional properties of the fluid, and it is defined as $Tr = \eta_{ext}(\dot{\epsilon}) / \eta_0$, where η_{ext} is the extensional viscosity at an extensional strain rate $\dot{\epsilon}$ and η_0 is the zero-shear-rate viscosity. Arigo and McKinley [5] evaluated this quantity using a

characteristic strain rate $\dot{\epsilon} = \dot{\gamma}/\sqrt{3}$ for a shear-thinning polyacrylamide solution and for a constant viscosity polyisobutylene solution, and found that a high value of this parameter correlates with the presence of a negative wake. This criterion also explains the lack of negative wake in highly elastic Boger fluids [8,9], where De/Tr is relatively small. These fluids exhibit an “extended wake” behind the sphere, but the velocity throughout the wake is positive (i.e., in the same direction as the sphere motion).

The transient behavior of the sphere sedimentation has also received much attention. While most studies focused on the initial sphere acceleration upon release [10–12], Bisgaard [13,14] reported that the flow in the wake of the sphere could become time-dependent at high Deborah number (> 40) in a solution of polyacrylamide and glycerol. However such fluctuations in wake velocity have not been observed in polymer solutions by other researchers [4,5]. In contrast, in wormlike micellar fluids, fluctuations in the velocity in the wake as well as in the sphere settling velocity have been reported repeatedly by multiple groups [15–17].

Wormlike micellar (WLM) fluids are surfactant solutions in which the surfactant monomers self-assemble into elongated micelles. They have found many applications ranging from cosmetic products to enhanced oil recovery [18]. Similar to polymer chains, the WLM chains form entangled networks in solution, which give rise to the viscoelasticity of the WLM fluids [19]. The main difference between WLM and polymer chains is that, unlike a covalently bonded polymer backbone, wormlike micelle chains are self-assembled by weaker interactions. As a result, the micelles are constantly breaking and reforming in solution at equilibrium (and for this reason WLM fluids are sometimes called “living polymers”). The transient nature of the micelle network leads to several unique rheological properties of the WLM fluids. It has been shown that for a broad range of surfactant chemistry, concentration and temperature, the linear viscoelasticity of WLM fluids follows a single model Maxwell model [19–21], making these fluids ideal model fluids for rheological research. Cates and co-workers [22,23] successfully explained such rheological behavior in terms of a reptation-reaction model. In the non-linear viscoelasticity regime, WLM fluids often exhibit shear banding (signified by a stress plateau in the steady shear flow curve) [24–26] or shear induced structure formation (signified by shear thickening) [27]. Under extensional deformation, the micelle chain extension and subsequent

breakage of micelle chains leads to initial strain hardening followed by an abrupt decrease in extensional viscosity [28] or filament rupture (in filament stretching experiments) [29,30].

In wormlike micellar fluids, Belmonte and co-workers [16,31,32] observed steady motion of settling spheres and rising bubbles when the terminal velocity and hence the characteristic velocity gradient $\Gamma = V_s/d$ was sufficiently small. However, above some critical velocity gradient they observed unsteady motion of settling spheres and rising bubbles, where the velocity of a sphere or bubble never reaches a constant terminal velocity but rather fluctuates throughout the sedimentation (or bubble rising) process. In a surfactant solution of cetyltrimethylammonium bromide (CTAB) and sodium salicylate (NaSal), Jayaraman and Belmonte [16] found a transition from steady to unsteady sphere sedimentation. At the onset of this transition, the critical velocity gradient, $\Gamma = V_s/d$, corresponds to a shear rate within the stress plateau in steady shear rheology measurements. This observation suggested that the flow instability was related to the formation of flow induced structure and/or shear banding in WLM fluids. Chen and Rothstein [17] studied unsteady sphere sedimentation in a CTAB-NaSal solution of a different concentration, using particle image velocimetry and flow-induced birefringence techniques. As in the studies of Belmonte and co-workers, they also observed steady sphere motion at low shear rates, and they measured negative wakes similar to those observed for shear-thinning solutions of linear polymers. Beyond some critical shear rate, Chen and Rothstein [17] also found a transition to unsteady sphere settling. They concluded that the flow instability likely resulted from a breakdown of the micelle network in the strong extensional flow in the negative wake region. The PIV measurements provided no observable evidence of shear banding in the flow field around the falling sphere, though the fluid was likely shear banding in steady shear flow. The possible effect of shear banding on the unsteady sphere sedimentation thus remains unclear. This study uses WLM solutions that are non-shear-banding, so that any possible shear-banding effects can be decoupled from the sedimentation dynamics.

In the study by Chen and Rothstein [17], the onset of unsteady sphere motion was found to correlate with a critical shear Deborah number $De_{s,crit} \approx 4$ at $Re \approx 10^{-4}$. Here the shear Deborah number and Reynolds number in the unsteady case are defined using an average sphere velocity, \bar{V}_s , i.e. $De_s = \bar{V}_s \lambda_s / d$ and $Re = \rho_f \bar{V}_s d / \eta$. On the other hand, recent work by

Mohammadigoushki and Muller [15] showed that the shear Deborah number was not sufficient as a criterion for the steady to unsteady transition. In CTAB-NaSal solutions with two concentrations and five temperatures, the transition takes place over a broad range of De_s . This observation is supported by the large variation of critical De_s reported in the literature, as summarized in Table 1. Mohammadigoushki and Muller [15] proposed using an extensional Deborah number, $De_{ext} = \dot{\epsilon}_m \lambda$, as a suitable criterion for the onset of flow instability. De_{ext} is defined locally in the strong extensional flow in the negative wake, where $\dot{\epsilon}_m$ is the maximum value of the extension rate, and it was shown to clearly distinguish between steady and unsteady sedimentation. A similar local extensional Deborah number was also used by Moss and Rothstein [33] in studying elastic instabilities in WLM fluid flow past a fixed cylinder. In both studies, unsteady flows were observed in CTAB-NaSal solutions. The validity of De_{ext} as an instability criterion in other surfactant systems remains an open question. One of the objectives of this study is to quantitatively examine the unsteady sphere sedimentation in two additional wormlike micelle systems, and test the universality of De_{ext} as a criterion for onset of flow instability.

Table 1. Summary of literature on sphere sedimentation in wormlike micelle fluid

Solution	Conc. [mM]	Shear banding?	Setup	Critical De_s	Periodic?	Ref
CTAB-NaSal	9/9, 25/25	Y	Sphere	$\sim 10^2 (De_{ext})$	N	[15]
	9/9	Y	Sphere	~ 40	N	[16]
	50/50	Y	Sphere	3.8	N	[17]
	10/10-80/80	Some	Sphere	Not available	Some	[34]
	50/50	Y	Cylinder	4.5	N	[33]
	8/8-11/11	Y	Bubble	~ 500	Y	[31]
CpCl-NaSal in brine	100/50/100	Y	Cylinder	Always stable	N/A	[33]
CpCl-NaSal	4/4-40/40	Some	Bubble	Not available	Y	[32]
CTAT-NaCl	42/100	Y	Sphere	5	Y	[35]

Another open question upon surveying the literature is regarding the periodicity of the velocity fluctuations of the sphere center of mass. As summarized in Table 1, while most studies reported that the velocity fluctuations were chaotic (mainly ones in CTAB-NaSal solutions), a few studies showed periodic or quasi-periodic velocity variations over time. Belmonte [31] found that rising bubbles in CTAB-NaSal solutions experience regular, periodic bursts in velocity, and showed the velocity variation is coupled with bubble deformation (cusp formation). Kumar et al. [35] reported that in two cetyltrimethylammonium p-toluenesulfonate (CTAT) - NaCl solutions, the unsteady sphere sedimentation manifests as periodic large bursts in sphere velocity, each followed by a higher frequency oscillatory velocity decay (similar to our results in Figure 4(a) at $De_s = 35.4$ shown below). Kumar et al. [35] proposed a theoretical model that suggests the observed dynamics were the result of periodic variations in flow induced structure formation of the wormlike micelle networks. However, a detailed, more quantitative experimental comparison of periodic and chaotic unsteady sphere sedimentation is needed to fully understand the flow instability.

This study is aimed at addressing the three aforementioned questions in unsteady sphere sedimentation: 1) does shear banding of the WLM fluids play a significant role in unsteady sedimentation? 2) Is the local extensional Deborah number De_{ext} a more suitable and universal criterion for flow instability than the shear Deborah number De_s ? 3) What is the underlying mechanism in determining the periodicity of sphere velocity fluctuations? These questions are investigated through a series of sphere sedimentation experiments with varying sphere size and density. To complement the extensive work in mostly shear-banding CTAB-NaSal solutions [15–17], we chose two non-shear-banding WLM fluids with different surfactant chemistry: a CTAT-NaCl and a CpCl-NaSal solution. The sedimentation of a single sphere at low confinement ratio (sphere to bounding cylinder diameter ratio) is analyzed with a combination of rheometry (both shear and extensional), sphere trajectory tracking, and PIV, in order to gain more insight into how sphere sedimentation in WLM fluids transitions from steady to unsteady, and from periodic to chaotic.

2. Materials and methods

2.1 Wormlike micellar solutions

Two wormlike micelle solutions were prepared using two different surfactant and salt combinations. The first test solution consisted of 10 mM of the cationic surfactant cetylpyridinium chloride (CpCl, Spectrum Chemical), and 15 mM of the salt sodium salicylate (NaSal, Spectrum Chemical). The second solution was made of 22 mM (1%wt.) of another cationic surfactant, cetyltrimethylammonium p-toluenesulfonate (CTAT, Sigma-Aldrich), with 50 mM of a different salt, sodium chloride (NaCl, Fisher Scientific). All chemicals were used as received. The solutions were prepared in deionized water and mixed using a magnetic stirring bar at around 50°C. Once the solutes were fully dissolved, the solutions were left undisturbed until all visible air bubbles had risen out of the solutions. It is well-documented that the pyridine ring in CpCl can undergo photo-induced ring cleavage and that the cleavage affects the rheology of the micellar solution [36], so efforts were made to minimize the light exposure of the CpCl-NaSal solution during preparation, storage and experiments.

To allow particle image velocimetry (PIV) measurements, the test solutions were also seeded with spherical metallic coated particles (TSI Inc.). The particles have a mean diameter of 12 μm and density of 2.6 g/cm^3 . The seeding concentration is kept low at <0.02%wt. The rheological properties of the solutions are unaffected by the addition of seeding particles at this concentration.

2.2 Shear rheology

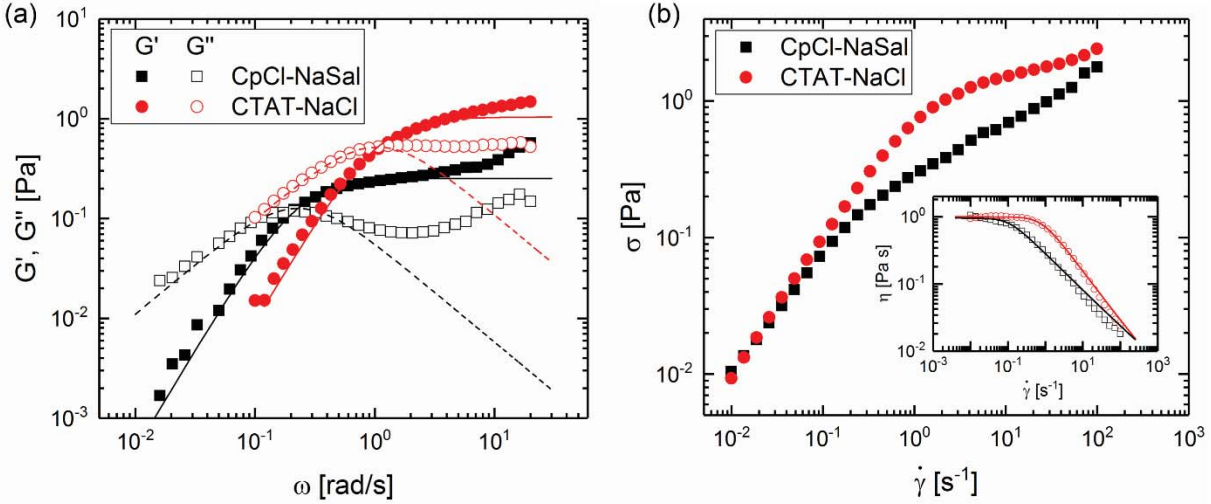


Figure 1. (a) Small amplitude oscillatory shear rheology for the two wormlike micelle solutions. Filled symbols (and solid lines) correspond to G' , open symbols (and dotted lines) correspond to G'' . The lines are the fit to a single mode Maxwell model. (b) Steady shear rheology for the two solutions.

The shear rheology of the two test solutions was characterized using a stress-controlled rheometer (Malvern-Gemini). All measurements were carried out at 22.5°C, using a Couette geometry (inner cylinder diameter 25 mm and outer cylinder diameter 27 mm).

The small amplitude oscillatory shear (SAOS) results are shown in Figure 1(a). The storage and loss moduli, G' and G'' , of the two solutions were each fitted using a single mode Maxwell model. Only results from lower frequencies (<1 rad/s) were used in the fit, as higher frequency results deviate from model predictions significantly, which is well-documented in the literature [37]. The shear relaxation times and plateau moduli obtained through fitting are listed in Table 2.

Table 2. Shear rheology of wormlike micelle solutions

Sample	Concentration	Maxwell model		Carreau model		
		G_0 [Pa]	λ_s [s]	η_0 [Pa s]	λ [s]	n
CpCl-NaSal	10mM/12mM	0.25	4.36	0.96	9.37	0.45
CTAT-NaCl	22mM/50mM	1.38	0.95	1.00	1.25	0.26

The results from steady shear measurements are shown in Figure 1(b). No apparent stress plateaus are observed in the data when plotted as shear stress versus shear rate, indicating that neither solution is shear banding under steady shear flow. As noted in Section I, previous studies of a sphere settling in wormlike micelle solutions have focused on shear banding systems; the two non-shear-banding solutions considered here allow us to examine the effect (or lack thereof) of shear banding on the dynamics of sphere sedimentation. The inset of Figure 1(b) shows the shear viscosity of the solutions as a function of shear rate. Both solutions are strongly shear thinning. The shear-rate-dependent viscosity is well-fitted for both solutions using the Carreau model:

$$\eta(\dot{\gamma}) = \eta_\infty + (\eta_0 - \eta_\infty) \left[1 + (\lambda_c \dot{\gamma})^2 \right]^{\frac{n-1}{2}} \quad (1)$$

where η_0 is the zero shear rate viscosity, η_∞ is the infinite shear rate viscosity (fixed as the viscosity of water), n is the power-law index, and λ_c is the Carreau relaxation time. These fitting parameters are also listed in Table 2. The zero-shear-rate viscosities and relaxation times from the Carreau fit are in reasonable agreement with those calculated from the Maxwell fit. In the discussion below, we used the shear relaxation times obtained from the Maxwell model to calculate the shear Deborah number $De_s = \bar{V}_s \lambda_s / d$, and the Carreau model parameters were used in calculating the shear-rate-dependent viscosity, $\eta(\dot{\gamma})$, which goes into computing $Re = \rho \bar{V}_s d / \eta(\dot{\gamma})$.

2.3 Modified Dripping onto Substrate (DoS) extensional rheology

The importance of the extensional rheology of wormlike micelle solutions in flow past a sphere has been noted in previous work [15,17]. Here we used a modified Dripping onto Substrate (DoS) setup to evaluate the extensional rheology of the test solutions. The DoS protocol was developed by Dinic et al. [38,39], and has been utilized to characterize the extensional rheology of various complex fluids, including dilute and semi-dilute polymer solutions [38,40] and DNA suspensions [41]. The protocol monitors the capillary thinning and pinch-off dynamics of a stretched liquid bridge formed by dispensing a drop from a nozzle to a solid substrate. For a viscoelastic fluid, the thinning dynamics exhibit an elasto-capillary regime, where the driving capillary stress is balanced by the elastic tensile stresses. This force balance leads to an exponential decay of the minimum radius of the liquid bridge [42]:

$$\frac{R(t)}{R_0} \propto \exp\left(-\frac{t}{3\lambda_{ext}}\right) \quad (2)$$

where R_0 is the outer radius of the nozzle (in our experiment $R_0 = 2\text{mm}$), and λ_{ext} is the extensional relaxation time. λ_{ext} can therefore be measured experimentally by monitoring the evolution of a liquid thread radius over time in the elasto-capillary regime.

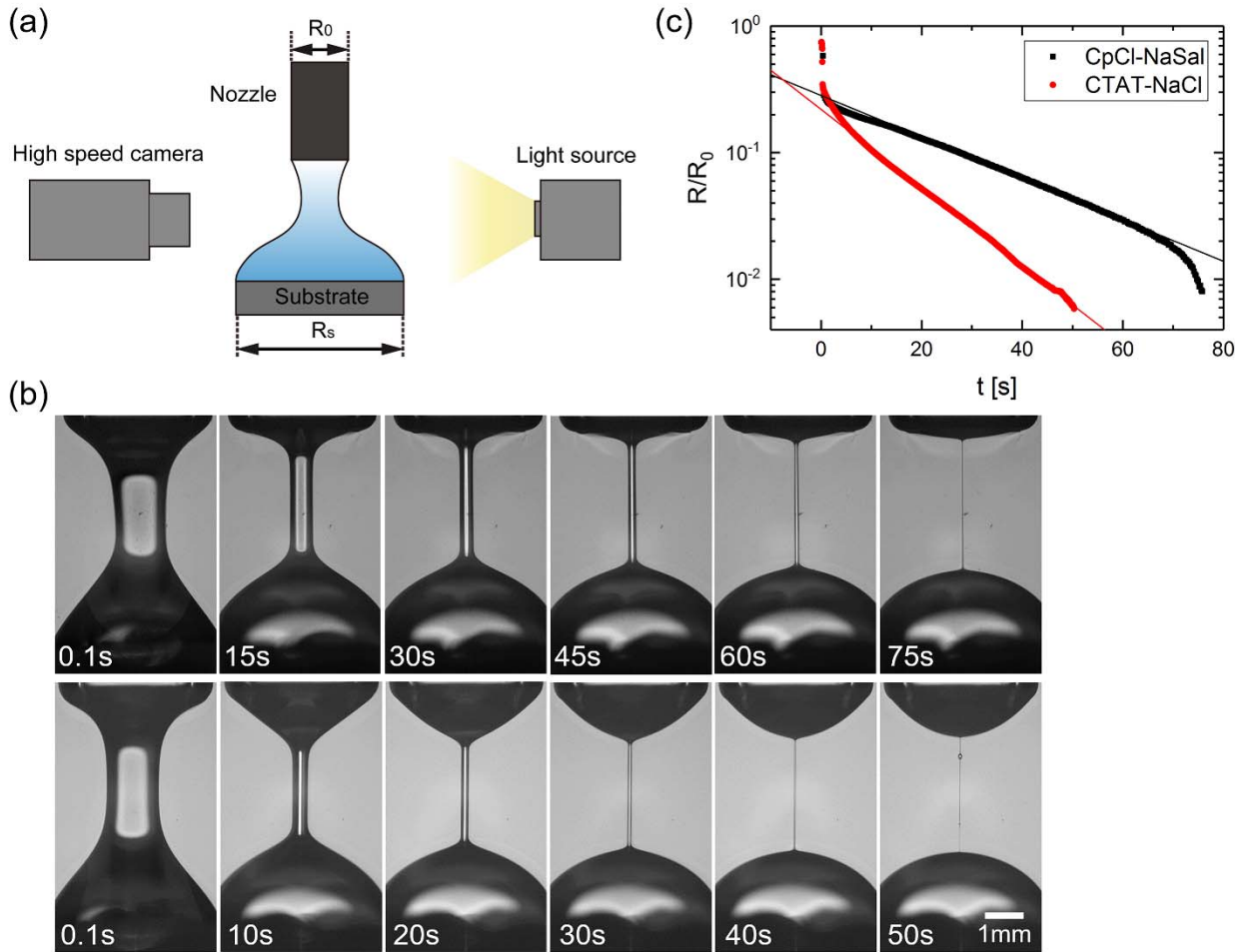


Figure 2. (a) Schematic diagram of the Drizzling onto substrate (DoS) experiment. (b) Sample images of the filament thinning from the DoS experiment for the CpCl-NaSal solution (top) and CTAT-NaCl solution (bottom). (c) The radius of the filament neck, non-dimensionalized with the nozzle radius, as a function of time during the thinning process for the two solutions. The solid lines indicate the best fits to Equation (2).

A schematic diagram of the experimental setup is shown in Figure 2(a). Unlike the original design of DoS using a large substrate (much larger than the drop size) [38], here we use a finite size circular substrate ($R_s = 2.5\text{mm}$) to pin the contact line of the sessile drop. This modification is necessary due to the low surface tensions of the surfactant micelle solutions used, which lead to high spreading coefficients on the substrate and a prolonged complete wetting process. The pinned contact line helps to decouple the capillary thinning dynamics from the drop spreading. The DoS process from initial drop contact with the substrate to the eventual pinch-off is recorded with a camera (Phantom M310) at 24 frames per second with backlighting of the

liquid filament. In Figure 2(b), montages of images from the DoS experiment are shown for the two test solutions. The capillary thinning and drop spreading are indeed decoupled: the initial spreading of the sessile drop is completed within the first few seconds, while the liquid bridge thinning and eventual pinch-off take about one minute. The cylindrical shaped liquid thread formed during the process is a characteristic of the elasto-capillary thinning regime [39,43].

Table 3. Extensional relaxation time of wormlike micelle solutions

Sample	Concentration	λ_{ext} [s]	λ_{ext}/λ_s
CpCl-NaSal	10mM/12mM	22.5 ± 3.6	5.2
CTAT-NaCl	22mM/50mM	12.6 ± 1.3	13.4

Figure 2(c) shows the semi-log plot of neck radius R vs. time t for both test solutions. The linear elasto-capillary regime is clearly observed for each solution after initial drop spreading. The deviation from the linear scaling at the final stage in CpCl-NaSal could be attributed to finite extensibility of the wormlike micelle chains. The extensional relaxation times extracted from the linear regime are listed in Table 3. The ratios of extensional to shear relaxation time, λ_{ext}/λ_s , are larger than 1 for both solutions. This is somewhat in agreement with results from capillary breakup extensional rheometer (CaBER) reported by Sachsenheimer et al.[44]. They observed the regime $\lambda_{ext}/\lambda_s \gg 1$ at low surfactant concentration (similar to the concentration used in this study), and attributed the large ratio to extension induced structure (EIS) build-up. However, they reported that EIS fluids also exhibited shear-induced structure (SIS) formation in shear flow, while our two solutions did not show the signature (sudden shear thickening at a critical shear rate) of SIS in shear rheology measurements.

It is also noted that pre-shearing or pre-stretching of wormlike micellar fluids can have a significant effect on the extensional rheology measured in FiSER (filament stretching extensional rheometry) or CaBER experiments, as shown by Rothstein and co-workers [45,46]. In the present study, the separation distance between the nozzle and the substrate was varied, thus varying the amount of pre-stretch before capillary thinning. The resulting relaxation times

remained relatively unchanged by varying the separation distance, as indicated by the standard deviations reported in Table 3.

2.4 Sedimentation experiments

The test solution was loaded into a cylindrical glass column with inner diameter of 8.5 cm and vertical length of 75 cm. The solution temperature was maintained at 22.5°C by a recirculating, constant temperature water bath. Spheres were released from a drill chuck at the top of the fluid column. The drill chuck was mounted on a translation stage to ensure the spheres were released at the central axis of the column. Table 4 shows the list of spheres used in the experiment. The Reynolds and Deborah numbers in each experiment were varied by selecting different spheres of appropriate size and density. The diameters of the spheres d remained small compared to the diameter of the column D_c (with $d/D_c < 0.0747$), so that the effects of the column walls are negligible. More detailed descriptions of the experimental setup can be found elsewhere [9,15,47].

Table 4. List of spheres used in sedimentation experiments

Material	Density(g/cm ³)	Diameter (inch)
Tungsten carbide	14.95	1/16, 5/64, 3/32
Brass	8.47	1/16, 3/32, 1/8
Stainless steel	7.91	1/16, 3/32, 1/8, 3/16, 1/4
Synthetic ruby	3.98	3/32, 1/8, 3/16
Ceramic (Al ₂ O ₃)	3.95	1/8, 3/16, 1/4
Aluminum	2.7	1/8, 3/16, 1/4
Teflon	2.3	1/8, 3/16, 1/4
Delrin	1.4	1/4

Two different imaging configurations were used in the experiments, one for sphere tracking and one for detailed measurements of the velocity field. Schematic diagrams of the two setups are included in supplementary Figure S1 [48]. The sphere tracking setup uses ambient lighting and a CCD camera (COHU 4910) to record the entire sphere settling process at 30 frames per second. The sphere trajectory is then tracked with sub-pixel resolution using MOSAIC open source plugin in ImageJ [49]. The velocity field around a falling sphere is measured separately using a particle image velocimetry (PIV) setup. The tracer particles in the test solutions are illuminated by a sheet of Ar-ion laser light at a wavelength of 488 nm. A high speed camera (Phantom M310) is used to capture the motion of the tracer particles as the sphere falls through the field of view. The field of view for these experiments was typically set at a location about half of the distance from the top to the bottom of the column, in order to avoid transients associated with the initial sphere release. The size of the field of view is approximately 10cm by 6cm, with small adjustments based on the sphere size. Frame capture rates were varied from 24 to 1000 fps depending on the sphere settling velocity. We confirmed that these variations do not affect the PIV results. The PIV measurements were analyzed with the open source PIVLab toolbox in Matlab [50], and further analysis was carried out in Matlab with specially written codes.

3. Results

3.1 Sphere settling velocity

The sphere tracking setup was used to monitor the trajectory of a single sphere sedimenting under gravity; from the trajectory, the instantaneous sphere settling velocity, V_s , was calculated as a function of time. Figure 3(a) shows the settling velocity of three different spheres followed over time in the CTAT-NaCl solution. The 1/4'' Teflon sphere quickly reaches its terminal velocity after the initial transient upon sphere release, and then the settling velocity remains constant. This constant terminal velocity is used to determine that the Deborah number is relatively low ($De_s = 1$). In comparison, using a denser sphere (aluminum) with the same diameter results in a higher De_s (now determined using the mean settling velocity, \bar{V}_s), and leads to a drastic change in the sedimentation dynamics. The sphere no longer reaches a constant

terminal velocity, instead its velocity fluctuates throughout the sedimentation process, showing sudden acceleration and deceleration spikes in the velocity as a function of time. With an even denser (ceramic) sphere and therefore at higher De_s , the fluctuations in settling velocity persist, and the frequency at which the fluctuations take place is increased.

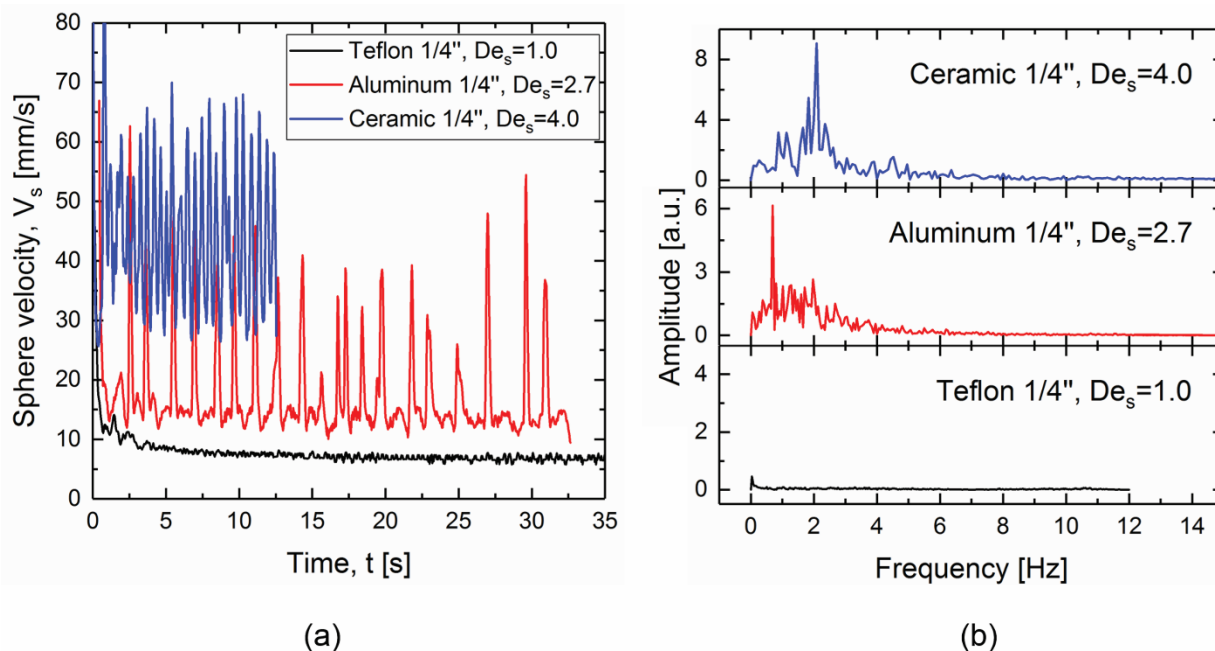


Figure 3. (a) The velocity of a sphere as a function of time as it settles in the CTAT-NaCl solution. Data for three spheres of different densities are shown. (b) The corresponding power spectra for the data in (a).

It is worth noting that the velocity fluctuations observed in the CTAT-NaCl solution show strong periodicity with most of the spheres tested, except at $De_s > 10$. The periodicity is evident from the power spectra of the velocity profiles shown in Figure 3(b). The periodic sedimentation is indicated by the single large, sharp peak in the frequency spectrum for both the aluminum and the ceramic spheres. Similar periodic sphere sedimentation was reported in the CTAT-NaCl wormlike micelle system by Kumar et al.[35], however the concentrations used by these authors differed from the present results.

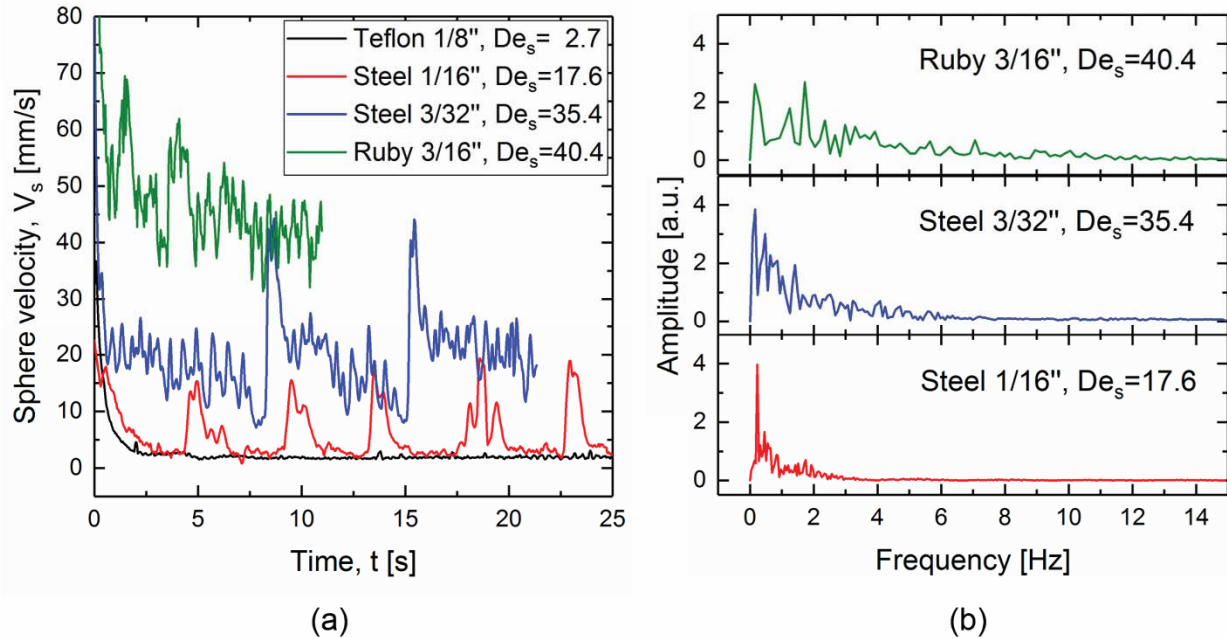


Figure 4. (a) The velocity of a sphere as a function of time as it settles in the CpCl-NaSal solution. Data for four spheres of different densities and/or size are shown. (b) The corresponding power spectra for the data in (a) for the three highest De_s .

For the CpCl-NaSal solution, the sedimentation velocity as a function of time for 4 different spheres is shown in Figure 4(a). Similar to the CTAT-NaCl solution, a transition from steady sphere sedimentation (with a 1/8" Teflon sphere) to periodic sedimentation (with a 1/16" stainless steel sphere) is observed. The periodicity is again indicated by the large, narrow peak in the frequency spectrum shown in Figure 4(b) (bottom panel). Due to the higher shear relaxation time (see Table 2) of the CpCl-NaSal solution, higher De_s can be accessed compared to the CTAT-NaCl case. At higher De_s , achieved with a 3/32" stainless steel sphere, velocity fluctuations were still quasi-periodic but with pronounced contributions from higher order frequencies. This is also evident from the frequency spectrum where there is considerable broadening of the peak due to these contributions. A further increase in De_s using the 3/16" ruby sphere resulted in a greater degree of irregularity in the velocity fluctuations and no recognizable periodicity, and a frequency spectrum with multiple peaks. In previous studies of unsteady sphere sedimentation (or bubble rising) in wormlike micellar fluids, periodic [31], periodic with higher order frequencies [34,35], and completely chaotic sedimentation [15,17] have all been reported separately in different micellar solutions. To the best of our knowledge, Figure 4

represents the first report of the change from periodic to progressively more irregular velocity fluctuations with increasing De_s in a single solution.

3.2 Flow field around the falling sphere

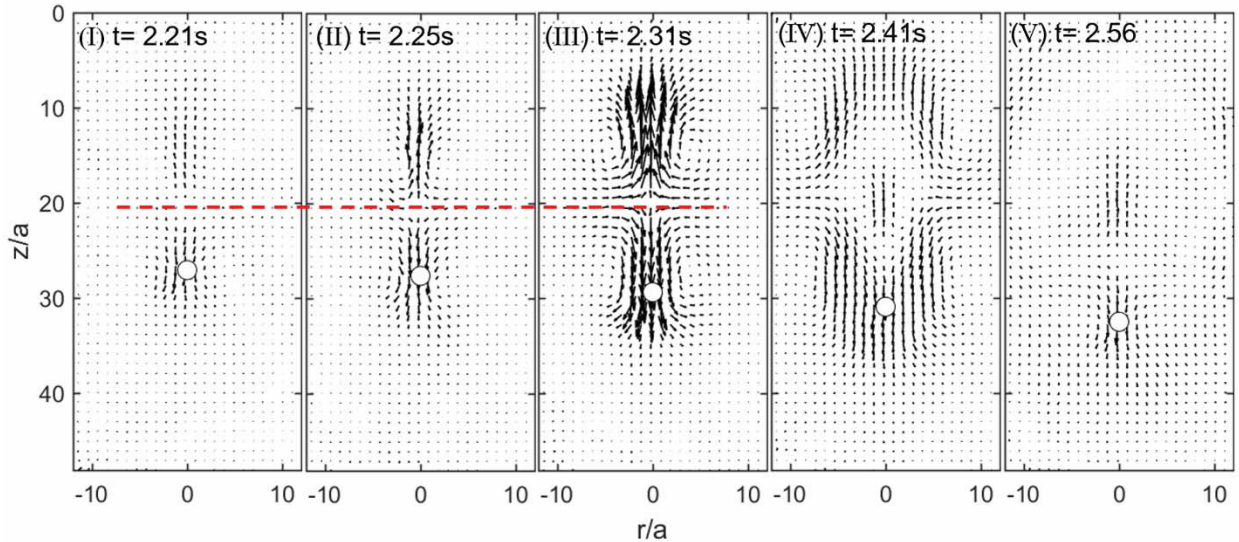


Figure 5. Velocity vector maps from PIV for flow around a 3/32" stainless steel sphere settling in CTAT-NaCl. The sedimentation is unsteady under these conditions; the average terminal velocity yields $De_s = 4.2$. Velocity vectors are scaled such that an arrow of length $l/a = 1/3$ corresponds to 1 mm/s, where a is the radius of the sphere.

Particle image velocimetry was used to characterize the flow field around the sphere as unsteady sedimentation takes place. Figure 5 shows a series of velocity vector fields during periodic sedimentation of a 3/32" stainless steel sphere in the CTAT-NaCl solution ($De_s = 4.2$). The series of plots is based on images captured during one velocity oscillation, with the time stamps showing the time elapsed from the instant when the sphere falls into the camera field of view. The velocity vectors are scaled such that an arrow of length $l/a = 1/3$ corresponds to a velocity of 1 mm/s, where a is the radius of the sphere. The complete movie showing motion of the sphere and fluid is provided in supplementary materials. Similar velocity vector plots have been presented by Chen and Rothstein [17] and Mohammadigoushki and Muller [15] for

wormlike micellar solutions of CTAB-NaSal. Consistent with their observations, Figure 5 clearly shows a negative wake region behind the falling sphere, which intensifies significantly as the sphere velocity starts to increase. The presence of the negative wake results in a strong extensional flow field behind the sphere. As the flow instability takes place and the sphere accelerates (Figure 5(I-III)), the stagnation point within the negative wake does not follow the downward moving sphere, rather it remains relatively stationary (indicated by the red dashed line in Figure 5). The enhancement of extensional flow is localized during sphere acceleration. This observation supports the hypothesis that the extensional flow in the negative wake leads to local breakage of the micelle network, and therefore causes the flow instability and unsteady sphere motion [15,17]. Once the sphere velocity decreases, as shown in Figures 5(IV-V), a restructured and weaker negative wake is established closer to the sphere. The stagnation point for this new wake remains a constant distance from the falling sphere, similar to the negative wakes observed in steady sphere sedimentation in both polymer [5] and wormlike micellar solutions [15,17], until the next rapid acceleration takes place. In addition, the strong burst in extensional flow during the acceleration forms an elastic wave, which propagates outwards and decays over time. The elastic wave is best observed in the movie included in supplementary materials. This wave can be clearly recognized in Figure 5(IV), but it becomes significantly weaker after ~ 0.15 s in Figure 5(V). The time scale of the wave dissipation is shorter compared to the sphere velocity oscillation period of ~ 1 s, therefore the next sphere acceleration period is hardly affected by this elastic wave.

The local velocity field may be further examined by following the vertical component of the fluid velocity, v_z , along the centerline of the sphere ($r/a = 0$). Figure 6(a) shows the velocity profiles corresponding to the flow fields shown in Figure 5. The profiles are shifted to v_z vs. $z' = (z - z_{sphere})/a$, where z_{sphere} is the position of the center of mass of the sphere, so that the sphere is always located at $z' = 0$. The fluid velocity behind the sphere ($z' < 0$) reaches negative values, indicating negative wake formation. The stagnation point (z' at which $v_z = 0$) appears to be moving further away from the sphere during sphere acceleration (II and III), which is a result of the localized flow enhancement shown in Figure 5(II-III). After the sphere acceleration, an additional negative velocity region further downstream from the sphere can be observed at time IV. This is due to the elastic wave formation and propagation.

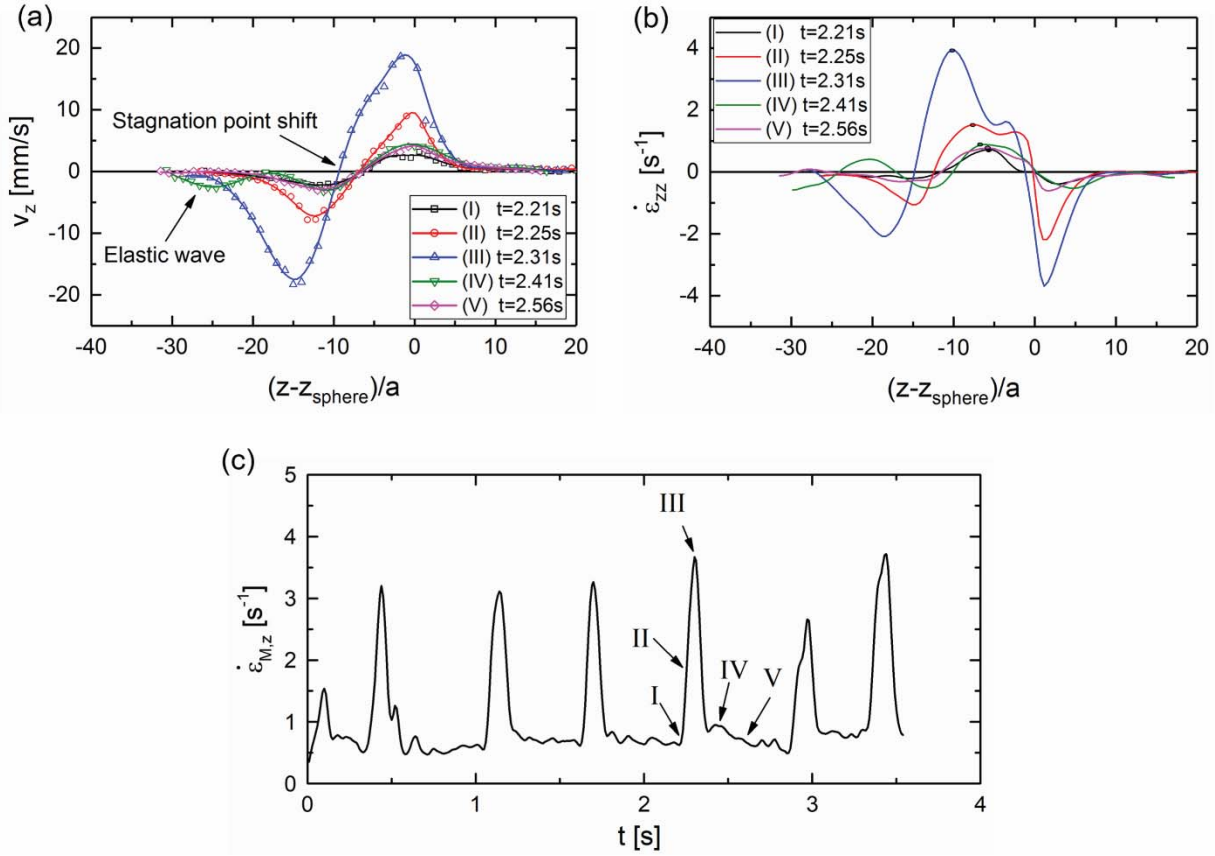


Figure 6. For flow around a 3/32” stainless steel sphere settling in CTAT-NaCl: (a) The axial velocity v_z in the fluid as a function of axial position. The axial position has been non-dimensionalized so that the center of mass of the sphere is always located at $(z-z_{\text{sphere}})/a = 0$. (b) The local extensional strain rate $\dot{\epsilon}_{zz}$, defined in equation (3), as a function of axial position. (c) The maximum strain rate, $\dot{\epsilon}_{M,z}$ as a function of time t . The points indicated I through V correspond to the times shown in Figure 5.

Mohammadigoushki and Muller [15] proposed an extensional Deborah number, De_{ext} , defined locally in the negative wake as $De_{\text{ext}} = \lambda \dot{\epsilon}_M$. Here $\dot{\epsilon}_M$ is the maximum value of the local extensional strain rate within the negative wake region, $\dot{\epsilon}_{zz}$, which is given by

$$\dot{\epsilon}_{zz} = \frac{\partial v_z}{\partial z} \quad (3)$$

Using Equation 3, $\dot{\epsilon}_{zz}$ was obtained by numerically differentiating the centerline velocity at each measurement time point. To reduce noise from the differentiation, the experimentally resolved velocity profiles were first smoothed using the cubic spline smoothing function *csaps* in Matlab (results shown as solid lines in Figure 6(a)). The calculated extensional strain rate profiles are plotted as $\dot{\epsilon}_{zz}$ vs. $(z - z_{sphere})/a$ in Figure 6(b). Here the strain rate is positive for regions that are extensional and negative for regions that are compressive. Moving downstream from the sphere, the centerline velocity decreases from the sphere sedimentation velocity to negative values behind the sphere, and the extensional strain rate becomes positive and increases until a maximum is reached near the stagnation point within the negative wake region. This instantaneous maximum strain rate, $\dot{\epsilon}_{M,z}$, was determined for each velocity profile and followed over time, as shown in Figure 6(c). The local maximum strain rate $\dot{\epsilon}_M$ is then obtained by taking the average of the peak values of $\dot{\epsilon}_{M,z}$ over the entire measurement window. The $\dot{\epsilon}_M$ in the case shown in Figure 6 is 3.4. Further discussion of the calculation of De_{ext} is presented in Section 4.1.

In the CpCl-NaSal solution, the transition from periodic to progressively more irregular sedimentation as De_s increases is shown by the sphere center-of-mass motion in Figure 4. Figure 7(a) presents another example of a quasi-periodic velocity profile obtained through sphere tracking of a 1/8'' ceramic sphere ($De_s = 16.4$). Each velocity oscillation period of ~ 5 s starts with one large velocity burst (primary velocity peak), which is followed by several oscillations with smaller amplitude at a higher frequency (secondary velocity peaks). Due to field of view constraints of the PIV measurement, we are not able to track the flow field over many oscillation periods. Instead, one primary and one secondary velocity peak is captured, and Figures 7(b-c) show the maximum strain rate and three velocity vector fields. In Figure 7(c) the velocity vectors are scaled such that an arrow of length $l/a = 1/5$ corresponds to a velocity of 1 mm/s. The instantaneous maximum strain rate $\dot{\epsilon}_{M,z}$ over time (Figure 7(b)) shows, similar to the sphere velocity profile (Figure 7(a)), a large, initial peak followed by a secondary peak that is smaller in magnitude. The fluid velocity vector plots (snapshots in Figure 7(c) and the full movie available in supplementary materials [48]) reveal that as the primary peak in strain rate forms, an elastic wave is produced by the strong burst in extensional flow, similar to the CTAT-NaCl case shown

in Figure 5(IV). The wave propagation appears slower than in the CTAT-NaCl solution. The slow wave propagation velocity is consistent with the smaller plateau modulus G_0 from the Maxwell model fit of the CpCl-NaSal solution, as the characteristic viscoelastic wave propagation velocity is given by $c = \sqrt{G_0/\rho}$ [51]. When the secondary velocity peak starts (Figure 7(c) III), the elastic wave from the primary peak is not completely dissipated and it remains in the proximity to the negative wake. Therefore, the dynamics of the secondary velocity peak could be significantly influenced by the interactions with this wave. The effect of elastic wave propagation on the periodicity of the sphere sedimentation is explored in more detail in Section 4.2.

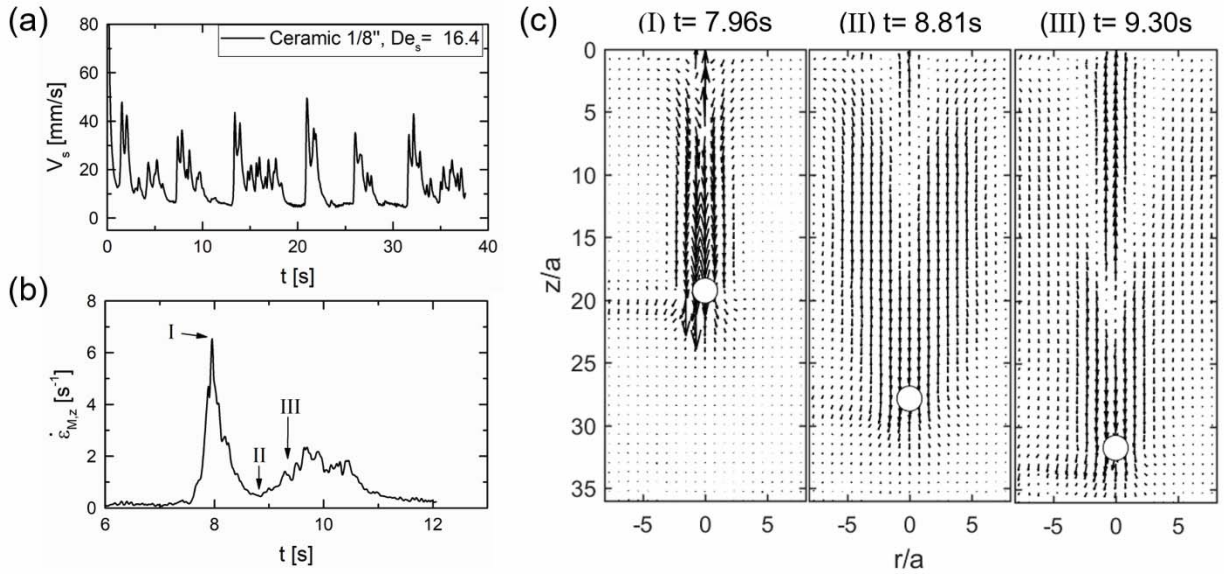


Figure 7. Unsteady sedimentation of a 1/8'' ceramic sphere in CpCl-NaSal; $De_s = 16.4$. (a) The center-of-mass motion of the sphere from particle tracking velocimetry as a function of time. (b) The instantaneous maximum strain rate $\epsilon_{M,Z}$ as a function of time obtained (as in Figure 6) from PIV measurements. (c) Velocity vector maps from PIV showing the velocity field at the three time points I-III indicated in (b).

4. Discussion

4.1 Criterion for unsteady sedimentation

From the sphere tracking results presented in Section 3.1, the shear Deborah number and Reynolds number (both defined in Section 1) may be calculated for all the spheres in both micellar solutions, the resulting De_s - Re phase diagram is shown in Figure 8(a). Here the steady sedimentation cases are shown as open symbols, while the unsteady cases are represented by filled symbols. A similar phase diagram was constructed for a CTAB-NaSal solution by Mohammadigoushki and Muller [15], and their results are also included in Figure 8(a). In agreement with the conclusion drawn in the CTAB-NaSal case [15], this parameter space fails to show a clear distinction between steady and unsteady sedimentation. Therefore, De_s alone cannot be used as a reliable criterion for predicting the occurrence of unsteady sedimentation.

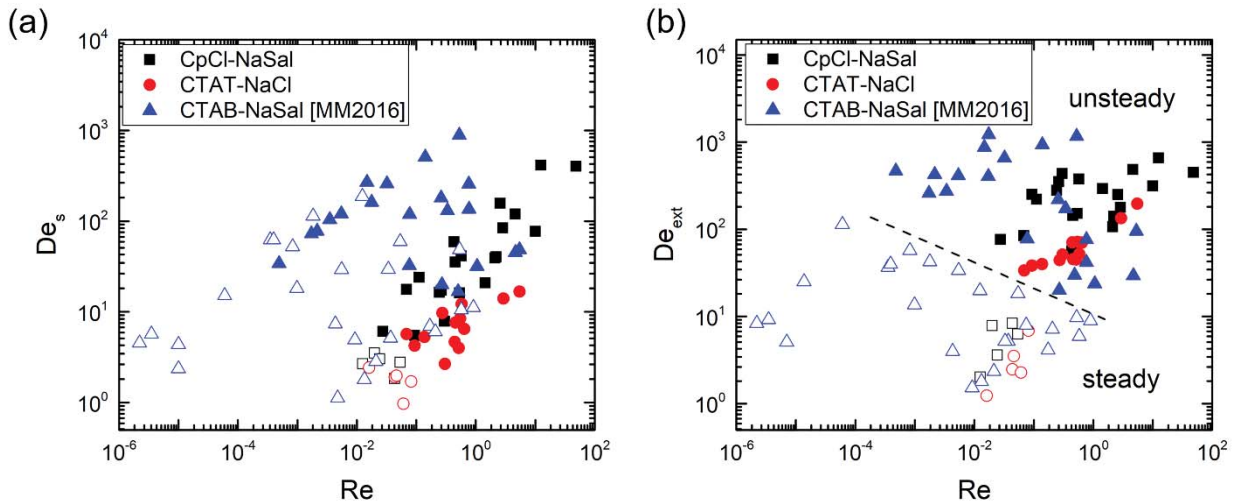


Figure 8. Sphere sedimentation experiments in CpCl-NaSal, CTAT-NaCl, and CTAB-NaSal (MM2016: ref [15]) plotted as (a) De_s versus Re and (b) De_{ext} versus Re . In both plots open symbols denote steady sedimentation, while filled symbols denote unsteady sedimentation.

In searching for a better criterion, Mohammadigoushki and Muller [15] showed that an extensional Deborah number, $De_{ext} = \lambda \dot{\epsilon}_M$, defined using the maximum local strain rate in the negative wake, is a suitable candidate. In the CTAB-NaSal solution studied, they used the shear relaxation time λ_s as the characteristic elastic time scale to calculate De_{ext} , citing disagreement in the literature characterization [30,44] of the extensional relaxation time λ_{ext} using capillary breakup extensional rheometer (CaBER). It was argued that since only CTAB-NaSal solutions

were studied, using λ_s instead of λ_{ext} would simply result in a shift of the entire dataset, and would not compromise the conclusion.

Here we continue to examine the validity of De_{ext} as the criterion for the steady-unsteady transition in different wormlike micellar systems. Since the solutions used in the present work show significantly different relaxation time ratios λ_{ext}/λ_s (Table 3), using the shear relaxation time as the characteristic time scale in extensional flow is no longer sufficient. However, the DoS protocol described in Section 2.3 provides an independent, consistent measurement of the extensional relaxation time λ_{ext} across different wormlike micelle solutions.

Figure 8(b) shows the phase diagram in $De_{ext}-Re$ parameter space, where $De_{ext} = \lambda_{ext}\dot{\epsilon}_M$, $\dot{\epsilon}_M$ is obtained from PIV measurements, and λ_{ext} is obtained from DoS measurements. Additional DoS measurements were carried out for the CTAB-NaSal solutions used by Mohammadigoushki and Muller [15]. For the CTAB-NaSal solutions, DoS experiments yield $\lambda_{ext}/\lambda_s \approx 1$, which is within the range of values reported by CaBER measurements [30,44]. Therefore the $De_{ext}-Re$ results for CTAB-NaSal in [15], which were based on λ_s , are included in Figure 8(b) without further shifting the data.

Figure 8(b) reveals a clear separation between steady and unsteady sedimentation for all three wormlike micellar systems. This supports the validity of using De_{ext} as a criterion for the flow instability. Remarkably, the critical De_{ext} appears to be a universal quantity. It is consistent across the different solutions tested, independent of the micelle composition, or the solution rheology (*e.g.* shear-banding or not). The only material property that plays a role is the extensional rheology of the solution characterized by λ_{ext} . This observation further strengthens the proposed physical picture that the flow instability is a direct result of micelle scission in the strong extensional flow in the negative wake [15,17,33]. Using an opposing jets extensional rheometer, Prud'homme and Warr [28] showed that the extensional viscosity of a wormlike micelle solution (tetradecyl trimethylammonium salicylate (TTASal) in NaSal) drops drastically above a critical extensional strain rate due to micelle scission. We speculate that in our experiments, a similar sudden decrease in the local extensional viscosity on reaching a critical strain rate (characterized by De_{ext}) leads to the acceleration of the sphere.

As shown by the dashed line in Figure 8(b), there appears to be a weak Re dependence on the value of the critical De_{ext} . It decreases from ~ 100 to ~ 10 as the Re increases from about 10^{-4} to 1, giving an apparent scaling of $De_{ext} \propto Re^{1/4}$. We speculate that increasing inertia may facilitate the breakage of the wormlike micelle network in extensional flow. We hope to systematically examine these factors and their impact on the unsteady sphere sedimentation in future work.

Finally, we note that an argument can be made that, since the maximum extension rate occurs following the onset of the elastic instability, a more appropriate onset criterion would be one based on the extension rate in the wake just prior to the onset of the elastic instability. Plots such as those shown in Figures 6c and 7b were used to identify $\dot{\epsilon}_{ext,base}$ and define $De_{ext,base} = \lambda_{ext} \dot{\epsilon}_{ext,base}$. A phase diagram in $De_{ext,base}-Re$ parameter space (similar to those in Figure 8) is included in supplemental materials as Figure S2(a) [48]. In general, unsteady cases correlate with higher $De_{ext,base}$, and steady cases correlate with lower $De_{ext,base}$. However, the separation between steady and unsteady cases is not as clear as it is in Figure 8(b). This may be related to experimental uncertainties in determining the baseline extension rate, which are suggested by some of the data in Figures 4(a) and 7(b), and by Figure S2(b) [48] in supplemental materials. In particular, in many unsteady cases no clear baseline is established, and the long time scale for the fluctuations in the sphere velocity coupled with the finite field of view in the PIV experiments leads to difficulties in determining a meaningful baseline strain rate.

4.2 Periodicity of unsteady sedimentation

In this section, we examine the periodicity (or lack thereof) of the sphere sedimentation in both CTAT-NaCl and CpCl-NaSal solutions. We follow the analysis shown in Figures 3 and 4 to obtain power spectra of the fluctuating sphere velocity profile for every unsteady sedimentation experiment. The frequency at which the highest amplitude peak appears is registered as the characteristic frequency of the velocity fluctuation. For each sphere, the sedimentation experiment was performed three times, and we found reasonable repeatability (within 10% error) in the characteristic frequency, even when the velocity fluctuations appear irregular.

The characteristic frequencies f are plotted against De_s and De_{ext} in Figure 9. Interestingly, the frequencies in both micelle solutions show a stronger correlation with De_s than with De_{ext} . While f shows a clear increasing trend with increasing De_s , the f versus De_{ext} plot displays much more scatter in the data. This appears to be in contradiction with the arguments in Section 4.1, where the importance of the extensional flow in the negative wake and the corresponding De_{ext} are highlighted. The correlation between f and De_s can be rationalized by recalling that the shear Deborah number is defined using the settling velocity averaged over the entire sedimentation process, *i.e.* $De_s = \lambda_s \bar{V}_s / d$. On the other hand De_{ext} is defined with the maximum local extensional strain rate $\dot{\epsilon}_M$, which is an instantaneous value. As a result, De_{ext} is better at characterizing the conditions for the instability onset, therefore a better criterion for the steady-unsteady transition. De_s may be a better measure of the overall flow strength of the entire unsteady sedimentation process, which is more closely related to the overall frequency of the settling velocity. An averaged extensional Deborah number defined using a mean extensional strain rate could, in principle, be an even better characterization of the sedimentation flow. However, it is experimentally challenging to capture the mean extensional strain rate, due to the limited field of view of the PIV measurements. More importantly, the extensional strain rate in the negative wake region is not only a function of time, but also decays over a long distance from the falling sphere (see Figure 6(c)). Therefore an extensional strain rate averaged over both time and spatial position is not very easily captured or calculated from experimental data.

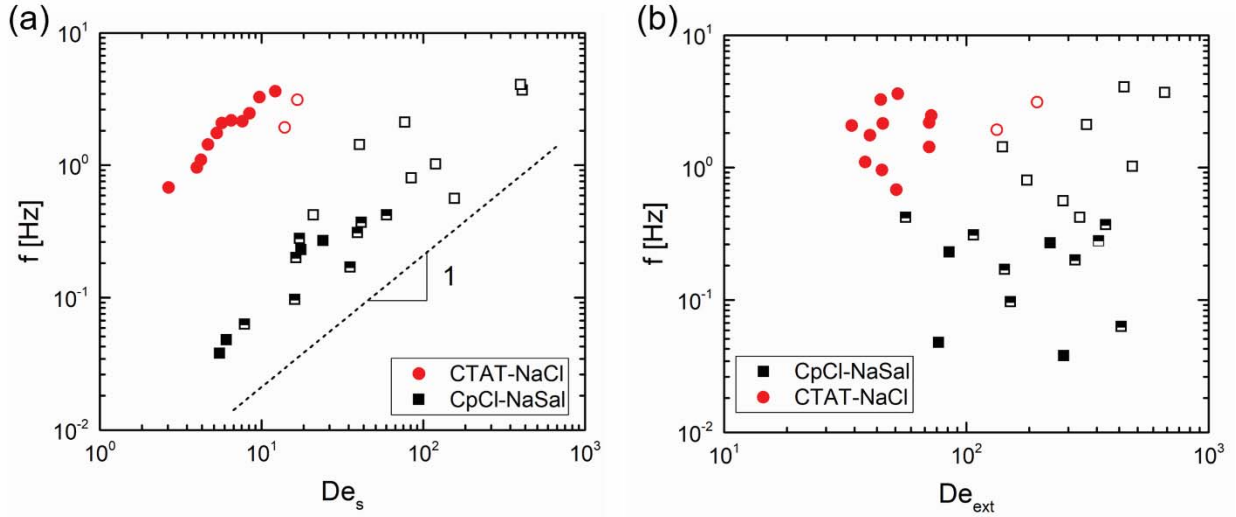


Figure 9. The characteristic frequency f of the sphere sedimentation velocity vs. Deborah numbers based on shear (a) and extension (b). Filled symbols: periodic, half-filled symbols: periodic but with high order frequencies, open symbols: irregular velocity fluctuations with no apparent characteristic frequency.

It is also worth noting that Figure 9(a) shows a scaling of power 1, *i.e.* $f \propto De_s$, for both micelle solutions. In dimensional terms, this linear dependence leads to

$$T\dot{\gamma} = \gamma_T = \text{constant} \quad (4)$$

Where $T = 1/f$ is the time period of each velocity oscillation and $\dot{\gamma} = \bar{V}_s/d$ is the characteristic shear rate. The product of the two, γ_T , provides a measure of the strain accumulated over one velocity oscillation, and it appears to be constant for each of the two solutions. In other words, during unsteady sphere sedimentation, the flow instability takes place when a critical strain is accumulated in each oscillation period. This is consistent with the instability being related to micelle breakage and with studies of wormlike micelle solutions in a filament stretching extensional rheometer (FiSER) [29,30]. In FiSER experiments, it was found that the filament ruptures at a constant critical Hencky strain, almost independent of the imposed strain rate. Moss and Rothstein [33,52] further correlated this critical strain in FiSER with the onset of instability in micellar flow past a single cylinder and a cylinder array. In the present study, we found that both the extensional strain rate and the accumulated strain play important roles: while the

dimensionless strain rate, De_{ext} , determines whether or not unsteady sedimentation occurs, the critical total strain γ_T determines how frequently the instability occurs.

Based on the power law fit of f versus De_s , the critical strain γ_T is calculated to be approximately 6.6 for the CTAT-NaCl solution and 26 for the CpCl-NaSal solution. There are no FiSER results available for these two exact solutions, however, for a series of CTAB-NaSal and CpCl-NaSal solutions, the critical Hencky strains in FiSER are reported to be in the range of 2 to 5 [17,29,30,33,52], significantly lower than the estimated γ_T here. The discrepancy could be due to two reasons: (1) in our study, γ_T is estimated based on the shear Deborah number De_s and the characteristic shear rate $\dot{\gamma}$. These parameters may be useful measures of the overall flow strength, but they are not quantitative measures for the strength of the extensional flow behind the sphere, and (2) unlike in filament stretching where the same fluid element is stretched over time, in sphere sedimentation the fluid element subject to the extensional flow is constantly changing as the sphere falls. Therefore the strain accumulated on a particular fluid element is only a fraction of the estimated value.

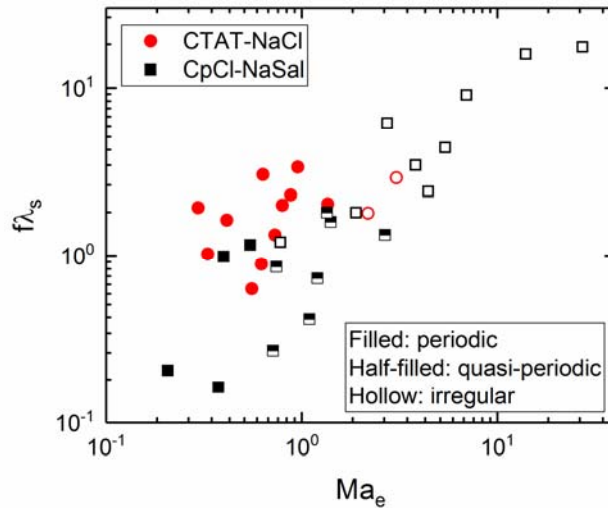


Figure 10. The characteristic frequency f non-dimensionalized with the shear relaxation time, as a function of the viscoelastic Mach number Ma_e

In Figure 9, we identified three types of sphere velocity fluctuations with different symbols: periodic, periodic but with significant contributions from higher order frequencies (quasi-periodic), and irregular. While the transition in the CpCl-NaSal solution involved the intermediate case involving higher order frequencies, in the CTAT-NaCl solution the transition is directly from periodic to irregular. A general trend shown in Figure 9(a) in both solutions is that as De_s increases, the velocity fluctuations become progressively less periodic. However, a clear distinction between the three types of behavior is not achieved based on the shear (or extensional) Deborah number. With the flow field measurements obtained from PIV (Figures 5 and 7), we recognized the important role played by the possible interaction between the flow instability in the negative wake (and the strong initial acceleration of the sphere) and the elastic wave generated from the previous instability. It could be that the elastic wave acts as a pre-shear or pre-stretch to the fluid element in the new negative wake. It is well-known that the extensional rheological properties of wormlike micelle solutions can be altered by pre-shear [45]. The pre-deformation from the elastic wave may result in the subsequent flow instability being different, and therefore more irregular velocity fluctuations. The effect of the elastic wave can be quantified using a viscoelastic Mach number, $Ma_e = \bar{V}_s / \sqrt{G_0/\rho}$, which compares the local flow velocity (characterized by \bar{V}_s) to the wave propagation velocity (characterized by $c = \sqrt{G_0/\rho}$). For Maxwell fluids such as the test wormlike micelle solutions, $G_0 = \eta_0 \lambda_s$ leads to $Ma_e = \bar{V}_s / \sqrt{G_0/\rho} = \sqrt{De_s Re_0}$, where Re_0 is the Reynolds number calculated using the zero shear viscosity. Figure 10 shows the scaled frequency $f \lambda_s$ as a function of Ma_e . The three types of velocity fluctuations are better separated using Ma_e , and for both solutions, the transition from periodic to more irregular velocity fluctuation happens at $Ma_e \sim 1$, which signifies the elastic wave becomes relevant to the sedimentation dynamics.

5. Conclusions

The unsteady sphere sedimentation in wormlike micellar fluids is studied in two different micellar solutions and for a range of sphere size and density. Using shear and extensional (by DoS) rheometry, sphere trajectory tracking and particle image velocimetry, we gained insights

into the three unanswered questions listed in Section 1 related to the effect of shear-banding on unsteady sphere sedimentation, the criterion for the steady to unsteady transition, and the periodicity of the sphere velocity fluctuation during unsteady sedimentation.

Consistent with several previous results in CTAB-NaSal micellar solutions [15–17], we showed that in a CTAT-NaCl solution and a CpCl-NaSal solution, some of the spheres never reach a constant terminal velocity when falling, instead the settling velocity fluctuates throughout the entire sedimentation process. Unlike many solutions used in the literature (see Table 1), the two solutions studied are not shear-banding in steady shear flow. This result suggests that shear-banding of a WLM fluid does not significantly affect the dynamics and flow instabilities in sphere sedimentation.

Regarding the transition from steady to unsteady settling, we found that an extensional Deborah number, De_{ext} , is a suitable dimensionless criterion for the flow instability. $De_{ext} = \lambda_{ext} \dot{\epsilon}_M$ is defined with the local maximum strain rate $\dot{\epsilon}_M$ in the negative wake region downstream of the falling sphere, which is determined from the flow field around the sphere measured by PIV, and the extensional relaxation time of the WLM fluid, which is determined by a modified Dripping onto Substrate (DoS) rheometry protocol. The critical De_{ext} onset of the flow instability is comparable across different micelle solution compositions and fluid rheology (*e.g.* shear banding or not), including previous results by Mohammadigoushki and Muller [15]. The universality of the critical De_{ext} suggests that the flow instability is mainly due to the strong extensional flow in the negative wake region, which may cause the micelle network to break down.

Depending on the solution and the sphere used, the fluctuations of the sphere settling velocity can be either periodic, quasi-periodic (periodic with significant higher-order frequency contributions), or irregular (no apparent periodicity), evidenced by the power spectrum of the settling velocity over time. The characteristic frequency of the velocity fluctuation is linearly correlated with the shear Deborah number $De_s = \lambda_s \bar{V}_s / d$, which is a measure of the average flow strength around the sedimenting sphere. This linear scaling suggests that a constant critical strain is accumulated in each period of the velocity oscillation. In general, the fluctuations are progressively more irregular with increasing De_s . By carefully examining the flow fields

obtained by PIV, we conclude that an elastic wave formed from one velocity oscillation may interact with the flow in the negative wake during the following velocity oscillation, and cause the oscillation to appear less periodic. The effect of this elastic wave is characterized by an elastic Mach number, $Ma_e = \bar{V}_s / \sqrt{G_0 / \rho}$, and more irregular velocity fluctuations are indeed observed when $Ma_e > 1$.

Overall, the dynamics of unsteady sphere sedimentation in WLM fluids appear strongly controlled by the flow in the negative wake region behind the falling sphere. The strong extensional flow within this region leads to transient micelle network breakdown, which may be the cause of the flow instability that leads to sphere velocity fluctuations and elastic wave propagation. We note that while the extensional flow in the wake plays a significant (if not dominant) role, other factors, such as the possibility of slip on the solid sphere surface and confinement effects (especially for the elastic wave), may also contribute. The effects of these other factors on the sedimentation flow stability, critical conditions, and the periodicity of fluctuations are left for future studies.

Acknowledgments

The authors gratefully acknowledge the financial support of this work by the National Science Foundation through award number NSF CBET 1335653. The authors also gratefully acknowledge Malvern Instruments for the loan of the Malvern Gemini rheometer.

References

- [1] R. Chhabra, *Bubbles, Drops, and Particles in Non-Newtonian Fluids*, Second Edition (2006).
- [2] L. G. Leal, M. M. Denn, and R. Keunings, Lake arrowhead workshop special issue papers—introduction, *J. Nonnewton. Fluid Mech.* **29**, 1 (1988).
- [3] G. G. Stokes, On the effect of the internal friction of fluids on the motion of pendulums, *Math. Phys. Pap.* **9**, 1 (1851).
- [4] G. H. McKinley, Steady and transient motion of spherical particles in viscoelastic liquids,

in *Transport Processes in Bubbles, Drops & Particles*, edited by R. P. Chhabra and D. De Kee (CRC Press, 2001), pp. 338–375.

- [5] M. T. Arigo and G. H. McKinley, An experimental investigation of negative wakes behind spheres settling in a shear-thinning viscoelastic fluid, *Rheol. Acta* **37**, 307 (1998).
- [6] O. G. Harlen, The negative wake behind a sphere sedimenting through a viscoelastic fluid, *J. Non-Newtonian Fluid Mech* **108**, 411 (2002).
- [7] M. B. Bush, On the stagnation flow behind a sphere in a shear-thinning viscoelastic liquid, *J. Non-Newtonian Fluid Mech* **55**, 229 (1994).
- [8] M. T. Arigo, D. Rajagopalan, N. Shapley, and G. H. McKinley, The sedimentation of a sphere through an elastic fluid. Part 1. Steady motion, *J. Nonnewton. Fluid Mech.* **60**, 255 (1995).
- [9] M. J. Solomon and S. J. Muller, Flow past a sphere in polystyrene-based Boger fluids: The effect on the drag coefficient of finite extensibility, solvent quality and polymer molecular weight, *J. Nonnewton. Fluid Mech.* **62**, 81 (1996).
- [10] M. D. Chilcott and J. M. Rallison, Creeping flow of dilute polymer solutions past cylinders and spheres, *J. Nonnewton. Fluid Mech.* **29**, 381 (1988).
- [11] D. Rajagopalan, M. . Arigo, and G. H. McKinley, The sedimentation of a sphere through an elastic fluid Part 2. Transient motion, *J. Nonnewton. Fluid Mech.* **65**, 17 (1996).
- [12] M. T. Arigo and G. H. Mckinley, The effects of viscoelasticity on the transient motion of a sphere in a shear-thinning fluid, *J. Rheol.* **41**, 103 (1997).
- [13] C. Bisgaard and O. Hassager, An experimental investigation of velocity fields around spheres and bubbles moving in non-Newtonian liquids, *Rheol. Acta* **21**, 537 (1982).
- [14] C. Bisgaard, Velocity fields around spheres and bubbles investigated by laser-doppler anemometry, *J. Nonnewton. Fluid Mech.* **12**, 283 (1983).
- [15] H. Mohammadigoushki and S. J. Muller, Sedimentation of a sphere in wormlike micellar fluids, *J. Rheol.* **60**, 1761 (2016).
- [16] A. Jayaraman and A. Belmonte, Oscillations of a solid sphere falling through a wormlike micellar fluid, *Phys. Rev. E - Stat. Nonlinear, Soft Matter Phys.* **67**, 065301/1 (2003).
- [17] S. Chen and J. P. Rothstein, Flow of a wormlike micelle solution past a falling sphere, *J. Nonnewton. Fluid Mech.* **116**, 205 (2004).
- [18] J. Yang, Viscoelastic wormlike micelles and their applications, *Curr. Opin. Colloid*

- Interface Sci. **7**, 276 (2002).
- [19] J.-F. Berret, Rheology of wormlike micelles: equilibrium properties and shear banding transitions, in *Molecular Gels: Materials with Self-Assembled Fibrillar Networks*, edited by R. G. Weiss and T. Pierre (Springer-Verlag, Berlin/Heidelberg, 2006), pp. 667–720.
- [20] M. E. Cates and S. M. Fielding, Rheology of giant micelles, *Adv. Phys.* **55**, 799 (2006).
- [21] L. M. Walker, Rheology and structure of worm-like micelles, *Curr. Opin. Colloid Interface Sci.* **6**, 451 (2001).
- [22] M. E. Cates, Reptation of living polymers: dynamics of entangled polymers in the presence of reversible chain-scission reactions, *Macromolecules* **20**, 2289 (1987).
- [23] M. E. Cates and S. J. Candau, Statics and dynamics of worm-like surfactant micelles, *J. Phys. Condens. Matter* **2**, 6869 (1990).
- [24] N. A. Spenley, M. E. Cates, and T. C. B. McLeish, Nonlinear rheology of wormlike micelles, *Phys. Rev. Lett.* **71**, 939 (1993).
- [25] E. Cappelaere and R. Cressely, Shear banding structure in viscoelastic micellar solutions, *Colloid Polym. Sci.* **275**, 407 (1997).
- [26] H. Mohammadigoushki and S. J. Muller, A flow visualization and superposition rheology study of shear-banding wormlike micelle solutions, *Soft Matter* **12**, 1051 (2016).
- [27] S. Lerouge and J. Berret, Shear-induced transitions and instabilities in surfactant wormlike micelles, in *Polymer Characterization: Rheology, Laser Interferometry, Electrooptics*, edited by K. Dušek and J.-F. Joanny (Springer, Berlin, Heidelberg, 2010), pp. 1–71.
- [28] R. K. Prudhomme and G. G. Warr, Elongational flow of solutions of rodlike micelles, *Langmuir* **10**, 3419 (1994).
- [29] J. P. Rothstein, Transient extensional rheology of wormlike micelle, *J. Rheol.* **47**, 1227 (2003).
- [30] A. Bhardwaj, E. Miller, and J. P. Rothstein, Filament stretching and capillary breakup extensional rheometry measurements of viscoelastic wormlike micelle solutions, *J. Rheol.* **51**, 693 (2007).
- [31] A. Belmonte, Self-oscillations of a cusped bubble rising through a micellar solution, *Rheol. Acta* **39**, 554 (2000).
- [32] N. Z. Handzy and A. Belmonte, Oscillatory rise of bubbles in wormlike micellar fluids with different microstructures, *Phys. Rev. Lett.* **92**, 124501 (2004).

- [33] G. R. Moss and J. P. Rothstein, Flow of wormlike micelle solutions past a confined circular cylinder, *J. Nonnewton. Fluid Mech.* **165**, 1505 (2010).
- [34] M. Kostrzewa, A. Delgado, and A. Wierschem, Particle settling in micellar solutions of varying concentration and salt content, *Acta Mech.* **227**, 677 (2016).
- [35] N. Kumar, S. Majumdar, A. Sood, R. Govindarajan, S. Ramaswamy, and A. K. Sood, Oscillatory settling in wormlike-micelle solutions: bursts and a long time scale, *Soft Matter* **8**, 4310 (2012).
- [36] M. A. Fardin, T. Divoux, M. A. Guedeau-Boudeville, I. Buchet-Maulien, J. Browaeys, G. H. McKinley, S. Manneville, and S. Lerouge, Shear-banding in surfactant wormlike micelles: elastic instabilities and wall slip, *Soft Matter* **8**, 2535 (2012).
- [37] J. Berret, J. Appell, and G. Porte, Linear rheology of entangled wormlike micelles, *Langmuir* **9**, 2851 (1993).
- [38] J. Dinic, Y. Zhang, L. N. Jimenez, and V. Sharma, Extensional relaxation times of dilute, aqueous polymer solutions, *ACS Macro Lett.* **4**, 804 (2015).
- [39] J. Dinic, L. N. Jimenez, and V. Sharma, Pinch-off dynamics and dripping-onto-substrate (DoS) rheometry of complex fluids, *Lab Chip* **17**, 460 (2017).
- [40] J. Dinic, M. Biagioli, and V. Sharma, Pinch-off dynamics and extensional relaxation times of intrinsically semi-dilute polymer solutions characterized by dripping-onto-substrate rheometry, *J. Polym. Sci. Part B Polym. Phys.* **55**, 1692 (2017).
- [41] K.-W. Hsiao, J. Dinic, Y. Ren, V. Sharma, and C. M. Schroeder, Passive non-linear microrheology for determining extensional viscosity, *Phys. Fluids* **29**, (2017).
- [42] V. M. Entov and E. J. Hinch, Effect of a spectrum of relaxation times on the capillary thinning of a filament of elastic liquid, *J. Nonnewton. Fluid Mech.* **72**, 31 (1997).
- [43] G. H. Mckinley, Visco-elasto-capillary thinning and break-up of complex fluids, *Rheol. Rev.* **1** (2005).
- [44] D. Sachsenheimer, C. Oelschlaeger, S. Müller, J. Küstner, S. Bindgen, and N. Willenbacher, Elongational deformation of wormlike micellar solutions, *J. Rheol.* **58**, 2017 (2014).
- [45] A. Bhardwaj, D. Richter, M. Chellamuthu, and J. P. Rothstein, The effect of pre-shear on the extensional rheology of wormlike micelle solutions, *Rheol. Acta* **46**, 861 (2007).
- [46] E. Miller, C. Clasen, and J. P. Rothstein, The effect of step-stretch parameters on capillary

- breakup extensional rheology (CaBER) measurements, *Rheol. Acta* **48**, 625 (2009).
- [47] D. Fabricsusan and J. M. Liepmann, Wake measurements for flow around a sphere in a viscoelastic fluid, *Phys. Fluids* **11**, (1999).
- [48] See Supplemental Material at [URL will be inserted by publisher] for additional information about the experiments and analysis.
- [49] X. Xiao, V. F. Geyer, H. Bowne-Anderson, J. Howard, and I. F. Sbalzarini, Automatic optimal filament segmentation with sub-pixel accuracy using generalized linear models and B-spline level-sets, *Med. Image Anal.* **32**, 157 (2016).
- [50] W. Thielicke and E. J. Stamhuis, PIVlab – towards user-friendly, affordable and accurate digital particle image velocimetry in MATLAB, *J. Open Res. Softw.* **2**, (2014).
- [51] L. E. Rodd, J. J. Cooper-White, D. V. Boger, and G. H. McKinley, Role of the elasticity number in the entry flow of dilute polymer solutions in micro-fabricated contraction geometries, *J. Nonnewton. Fluid Mech.* **143**, 170 (2007).
- [52] G. R. Moss and J. P. Rothstein, Flow of wormlike micelle solutions through a periodic array of cylinders, *J. Non-Newtonian Fluid Mech* **165**, 1 (2010).